
Semi-Analytical Solutions for Wave Propagation of Periodically Repetitive Schwarz Primitive Triply Periodic Minimal Surface Based Structure Embedded With Acoustic Black Hole Resonators

Yongbin Ma and Qingfeng Cheng

MIT Key Laboratory of Dynamics and Control of Complex Systems, Northwestern Polytechnical University, Xi'an 710072, PR China. E-mail: mayb@nwpu.edu.cn

(Received 15 February 2023; accepted 13 June 2023)

The Schwarz Primitive triply periodic minimal surface (P-TPMS) lattice structure is attracting more attention due to its superior mechanical properties and unique topological configuration. In this study, a new periodic configuration is proposed in which the unit cell is formed by embedding the acoustic black hole (ABH) component in the primary P-TPMS component. A semi-analytical method is developed to calculate the wave propagation properties of the proposed structure. The dynamical equilibriums of the primary P-TPMS and ABH components are described by the finite element method and the WKB method respectively. By considering the compatibility at the connections between the components and using the equivalent dynamic stiffness technique, dispersion analysis can be implemented in the framework of the wave and finite element (WFE) method. Various numerical examples with different number, type and connection position of the resonators are investigated. By comparing the calculation results from the present semi-analytical method with that from the finite element method, the effectiveness of the proposed method is validated. The influences of the number, type, and connection position of the resonators on the bandgap properties are investigated.

NOMENCLATURE

<i>P-TPMS</i>	Schwarz Primitive Triply Periodic Minimal Surfaces
<i>ABH</i>	Acoustic Black Hole
<i>WFE</i>	Wave and Finite Element
<i>TPMS</i>	Triply Periodic Minimal Surface

1. INTRODUCTION

Lightweight, load-bearing and vibration reduction structures are the eternal pursuit of various areas such as aerospace, automotive, civil, and naval engineering.¹ Cellular materials have been utilized frequently for these structures due to their remarkable high stiffness to weight ratio and porous characteristics.² Among them, triply periodic minimal surface (TPMS) based structures are attracting more and more attention along with the rapid development of additive manufacturing technology.³ A wealth of research work has been carried out on the performance of various aspects of the TPMS based structures.^{4–14}

The mechanical properties of different types of TPMS have been investigated experimentally and numerically. However, only a limited number of works can be found in the literature on the dynamic and wave propagation characters of TPMS based structures.^{15,16} Viet¹⁷ investigates the wave propagation characteristics of sheet and solid type triply periodic minimal surface structures, including the Gyroid, Primitive, Diamond, and IWP lattices over a broad range of relative density values. Viet and Zaki¹⁸ studies the free vibration and buckling characteristics of functionally graded porous beam with triply periodic minimal surfaces including Primitive, Diamond,

IWP, and Gyroid using Euler's beam theory. Simsek¹⁹ calculate the modal properties of additively manufactured TPMS structures using five different modeling methods for a beam. Yang²⁰ investigate the acoustic properties of additively manufactured TPMS-based structures. Elmadih²¹ predict the 1D bandgaps of beam-like surface-based lattices and demonstrate that TPMS lattice structures can induce mechanical bandgap behavior which can be used for manipulating elastic wave.

The wave bandgap of repetitive TPMS structure comes from the Bragg scattering mechanism, which is easy to achieve, and usually has a large bandwidth.²² However, for the Bragg scattering mechanism, the period of the structure repetitiveness has the same order of magnitude as the propagation wavelength, which means that a large system is required for the low-frequency band gap. Instead, a local resonant band gap is formed near the resonant frequency, which makes the unit cell size much smaller than the wavelength corresponding to the band gap.²³ Locally resonant metamaterials usually consist of a variety of materials. The discontinuous distribution of materials with different properties in complex spatial structures brings great challenges to manufacturing. Therefore, single-phase structures with subwavelength bandgaps are more practical in engineering practice and have attracted more and more attention in recent years.²⁴ In addition, Xiao²⁵ investigate the propagation of flexural waves in a locally resonant thin plate made of a two-dimensional periodic array of spring-mass resonators attached on a thin homogeneous plate. Miranda²⁶ investigate the complex band structure and forced response of flexural waves propagating in an elastic metamaterial thick plate. In order to produce more significant band gap characteristics compared with one resonator, structures with embed-

ded multi-resonators was presented which can lead to multiple resonant-type bandgaps with remarkable wave attenuation capabilities.²⁷⁻²⁹ As an alternative, a thin plate structure periodically attached with ABH beam resonators are proposed by Ma,³⁰ and multiple band gaps are obtained due to the multi-mode characteristic of ABHs. An ABH is a thin structure with a thickness that tapers according to a power law with an exponent greater than or equal to two. As the thickness diminishes, the entering waves slow down and their amplitude grows to infinity as the thinnest portion of the ABH is approached. Since the discovery of the ABH effect in 1988³¹ and the damping-layer treatment solution in 2004,³² a vast amount of research has been conducted into ABHs and verifies the advantage of ABHs in vibration reduction.³³⁻³⁸

Inspired by the remarkable porosity of the TPMS based structure and the multimode characteristic of the ABHs, a new configuration of which the unit cell is formed by embedding the ABH component in the primary P-TPMS component, where the ABH component plays the role of dynamic resonator, is proposed in this paper. The wave propagation properties of the proposed structure are calculated based on the dynamic equations of the unit cell. Up to now, various computational methods, including numerical and analytical methods, have been developed for the dispersion analysis of locally-resonant structures.³⁹⁻⁴³ By considering the complex geometry of the primary TPMS component, the analytical solution is obviously not applicable for the proposed configuration. As an alternative, the wave and finite element (WFE) method.⁴⁴⁻⁴⁶ can deal with periodic mediums with complex configuration since the mass and stiffness matrices can be obtained utilizing a commercial software package. However, the significant variable cross-section characteristics of the ABH component lead to a huge number of elements, which makes the WFE method face high computational cost. In this paper, a semi-analytical method is developed for the wave propagation analysis of the proposed new structural configuration. In the present method, the dynamic equation of the primary P-TPMS component is established by using the finite element method, and the higher-order WKB approach³⁸ is utilized to describe the flexural wave propagation within the ABH resonators. By considering the displacement-force relationship at the connections, an eigenproblem for the dispersion of the proposed configuration is established based on the wave propagation theory. Several numerical examples with different number, connection position and type of the resonators are considered. The effectiveness of the present semi-analytical method are validated by the WFE method. The bandgap property of these example structures are investigated.

2. GEOMETRY OF THE UNIT CELL AND PROBLEM DESCRIPTION

As shown in Fig. 1, the unit cell of the proposed periodic configuration was composed of the primary P-TPMS component which played a bearing role and the ABH component that was a dynamic resonator. For the sake of convenience, the bottom of the P-TPMS component was sealed, and the ABH component was connected to the P-TPMS component through a stiff bar that could be modeled by a spring for simplicity. The ABH component was constituted by two tapered beams, as shown in Fig. 1(e). Although only one resonator is shown

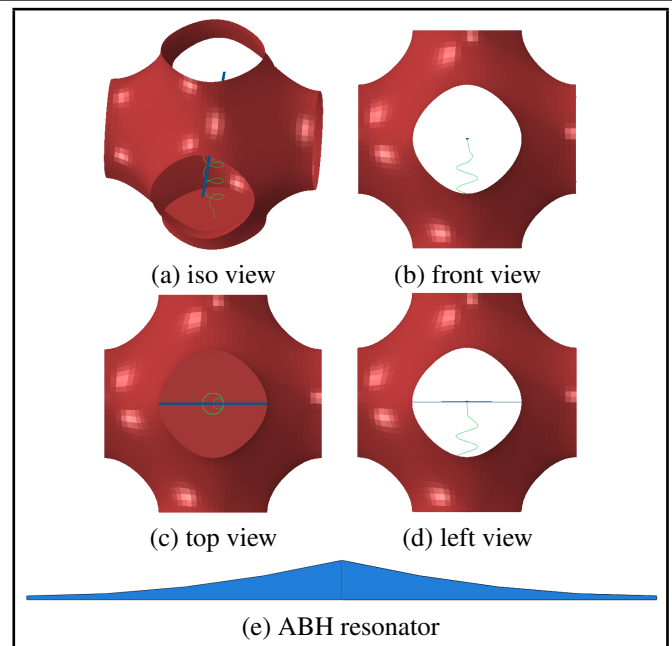


Figure 1. Configuration of the unit cell in different views: (a) iso view, (b) front view, (c) top view and (d) left view; (e) ABH component.

in Fig. 1 for clarity, the cases considering multiple resonators can be managed by the present method with no more difficulty and are investigated in the numerical examples.

As one kind of the TPMS structure, the P-TPMS is described by the following equation:

$$\phi_P(x, y, z) = \cos(\theta x) + \cos(\theta y) + \cos(\theta z) = s; \quad (1)$$

where $\theta = \frac{2\pi}{\Delta}$, Δ denotes the characteristic length of a unit cell, ϕ_P determined the pore type, x, y, z were spatial coordinates, and s happened for the network phase of the TPMS lattice. In the following analysis, the constant s was chosen as 0. Considering the complex surface, the dynamic problem of the primary P-TPMS component cannot be described analytically. In this work, the primary P-TPMS component was generated by the software MSlattice developed by Al-Ketan and Abu Al-Rub.⁴⁷ And then the commercial software ABAQUS was adopted to obtain the finite element model.

The ABH component consists of two parts, i.e. Part 1 and Part 2, as shown in Fig. 2. Both parts were tapered beams. For the sake of simplicity, only the flexural vibration along the y direction is considered here. Other geometrical parameters are also given in Fig. 2. The thickness function of Part 1 was expressed as $h_1(x) = \varepsilon_1 x^{\mu_1} + h_{tip}$, $x = 0..l$. The thickness function of Part 2 was described as $h_2(x) = \varepsilon_2(l-x)^{\mu_2} + h_{tip}$, $x = 0..l$, where $\varepsilon_i = \frac{(h_0 - h_{tip})}{l^{\mu_i}}$ with $i = 1, 2$ was a scaling factor, μ_i was the power of the taper that defined the gradient. The local coordinate is considered here whose origin is located at the left end of each part.

In this paper, wave propagation properties of the periodic structure is calculated based on the dynamic equilibrium equation of its unit cell. Traditionally, the finite element model of the unit cell can be established and then the classical WFE method can be used to calculate the dispersion properties. However, many elements and a consequently high computational burden will be induced by the ABH components due to their significant characteristic of variable thickness. To make efficient calculations, the dynamics of the ABH component is

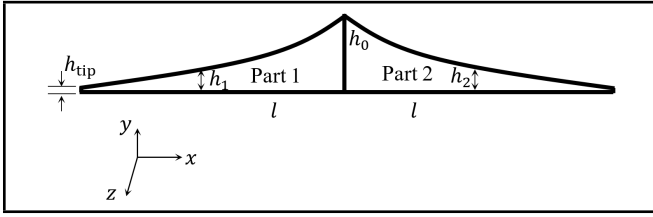


Figure 2. Geometry parameters of the ABH component.

described by using a general higher-order WKB approach³⁸ in this paper. The key step of the presented analysis framework is how to address the dynamic coupling between the primary P-TPMS component and the ABH components. To address this, the equivalent dynamic stiffness technic is utilized.

3. SEMI-ANALYTICAL SOLUTION FOR DISPERSION ANALYSIS

For the primary P-TPMS component, the dynamic equilibrium equation was formulated in the frequency domain as $\mathbf{D}\mathbf{q} = \mathbf{F}$, where \mathbf{q} and \mathbf{F} represent the displacement and force respectively. \mathbf{D} represents the dynamic stiffness matrix, and was expressed as $\mathbf{D} = -\omega^2\mathbf{M} + \mathbf{K}(1 + i\eta)$, where \mathbf{M} and \mathbf{K} were the mass and stiffness matrices, while η was the loss factor and ω was the angular frequency. By considering the connected degrees of freedom between the primary P-TPMS component and the ABH component, the dynamic equilibrium equation can be written as:

$$\begin{bmatrix} \mathbf{D}_{pp} & \mathbf{D}_{pc} \\ \mathbf{D}_{cp} & \mathbf{D}_{cc} \end{bmatrix} \begin{pmatrix} \mathbf{q}_p \\ \mathbf{q}_c \end{pmatrix} = \begin{pmatrix} \mathbf{F}_p \\ \mathbf{F}_c \end{pmatrix}; \quad (2)$$

where the subscript “c” meant the connected degrees of freedom, and subscript “p” referred to the other degrees of freedom of the primary P-TPMS component. The dynamic coupling relationship between the primary P-TPMS component and the ABH component can be expressed as:

$$\mathbf{k}_{eq}\mathbf{q}_c = \mathbf{F}_c; \quad (3)$$

where \mathbf{k}_{eq} was the equivalent dynamic stiffness provided by the ABH component. The derivations for \mathbf{k}_{eq} can refer to References.³⁰ The combination of Eq. (2) and Eq. (3) leads to:

$$\tilde{\mathbf{D}}\mathbf{q}_p = \mathbf{F}_p; \quad (4)$$

where $\tilde{\mathbf{D}} = (\mathbf{D}_{pp} + \mathbf{D}_{pc}(\mathbf{k}_{eq} - \mathbf{D}_{cc})^{-1}\mathbf{D}_{cp})$. Following the classical procedure of the WFE method,⁴⁴ Eq. (4) can be rewritten as:

$$\begin{bmatrix} \tilde{\mathbf{D}}_{II} & \tilde{\mathbf{D}}_{IL} & \tilde{\mathbf{D}}_{IR} \\ \tilde{\mathbf{D}}_{LI} & \tilde{\mathbf{D}}_{LL} & \tilde{\mathbf{D}}_{LR} \\ \tilde{\mathbf{D}}_{RI} & \tilde{\mathbf{D}}_{RL} & \tilde{\mathbf{D}}_{RR} \end{bmatrix} \begin{pmatrix} \mathbf{q}_{p,I} \\ \mathbf{q}_{p,L} \\ \mathbf{q}_{p,R} \end{pmatrix} = \begin{pmatrix} \mathbf{F}_{p,I} \\ \mathbf{F}_{p,L} \\ \mathbf{F}_{p,R} \end{pmatrix}; \quad (5)$$

where the subscript “I, L, R” indicated the degrees of freedom of internal region, left end and right end of the unit cell, respectively. Consider the method developed by Zhong and Williams,⁴⁸ let $\Phi = \begin{pmatrix} \mathbf{q}_{p,L} \\ \mathbf{F}_{p,L} \end{pmatrix}$ and $\Psi = \begin{pmatrix} \mathbf{q}_{p,R} \\ \mathbf{F}_{p,R} \end{pmatrix}$, and consider that there was no external force acting on the internal region of the unit cell, and then Eq. (5) leads to:

$$\begin{pmatrix} \mathbf{q}_{p,R} \\ -\mathbf{F}_{p,R} \end{pmatrix} = \mathbf{N}\Psi; \quad (6)$$

$$\Phi = \mathbf{L}\Psi; \quad (7)$$

where, $\mathbf{N} = \begin{bmatrix} \mathbf{0} & \mathbf{I} \\ \tilde{\mathbf{D}}_{RI}\tilde{\mathbf{D}}_{II}^{-1}\tilde{\mathbf{D}}_{IL} - \tilde{\mathbf{D}}_{RL} & \tilde{\mathbf{D}}_{RI}\tilde{\mathbf{D}}_{II}^{-1}\tilde{\mathbf{D}}_{IR} - \tilde{\mathbf{D}}_{RR} \end{bmatrix}$, $\mathbf{L} = \begin{bmatrix} \mathbf{I} & \mathbf{0} \\ \tilde{\mathbf{D}}_{LL} - \tilde{\mathbf{D}}_{LI}\tilde{\mathbf{D}}_{II}^{-1}\tilde{\mathbf{D}}_{IL} & \tilde{\mathbf{D}}_{IR} - \tilde{\mathbf{D}}_{LI}\tilde{\mathbf{D}}_{II}^{-1}\tilde{\mathbf{D}}_{IR} \end{bmatrix}$. By combining the displacement compatibility condition and force equilibrium condition at the coupling edge of two adjacent unit cells j and $j - 1$, i.e. $\Phi^j = \begin{pmatrix} \mathbf{q}_{p,R} \\ -\mathbf{F}_{p,R} \end{pmatrix}^{j-1}$ and the Bloch theory, i.e. $\begin{pmatrix} \mathbf{q}_{p,R} \\ -\mathbf{F}_{p,R} \end{pmatrix}^j = \lambda \begin{pmatrix} \mathbf{q}_{p,R} \\ -\mathbf{F}_{p,R} \end{pmatrix}^{j-1}$, generalized eigenvalue problem can be obtained as:

$$(\mathbf{L}^T\mathbf{J}\mathbf{N} + \mathbf{N}^T\mathbf{J}\mathbf{L})\Psi = (\lambda + \lambda^{-1})\mathbf{L}^T\mathbf{J}\mathbf{L}\Psi; \quad (8)$$

where, $\mathbf{J} = \begin{bmatrix} \mathbf{0} & \mathbf{I}_n \\ -\mathbf{I}_n & \mathbf{0} \end{bmatrix}$, $\lambda = e^{-ik\Delta}$, \mathbf{I}_n was unit matrix, n was the total number of degree of freedom of the left and the right coupling cross-section of the unit cell. The wave number k can be obtained by solving this equation.

4. NUMERICAL EXAMPLES

In this section, the wave propagation properties of three cases of example structures are investigated. For each case, two types of resonators are considered, i.e. spring-mass resonator and ABH resonator, and each resonator has the same mass. For all the cases, the total mass of the resonators was kept unchanged. For the first case, only one resonator was embedded in the primary P-TPMS component. The resonator was connected to the bottom surface of the unit cell at three nodes, respectively, i.e. nodes 3095, 3264 and 3268, through a stiff bar which was modeled by a spring, as shown in Fig. 3, and node 3264 was at the central of the bottom face of the TPMS component. For the second case, the two resonators were connected to nodes 3095 and 3264 of the primary P-TPMS component. For the third case, the three resonators were connected to the three nodes of the primary P-TPMS component, respectively. The thickness of the primary P-TPMS component was 3 mm. The geometrical parameters of the ABH beam were: $h_0 = 0.0025$ m, $h_{tip} = 0.00025$ m, $l = 0.2$ m, and $\mu_1 = \mu_2 = 2$. The material properties of the unit cell were: density was 1200 and 2700 kg/m³, Young’s modulus was 2 and 70 GPa for the TPMS and ABH component, respectively, and Poisson’s ratio is 0.3. For the first case, the spring-mass resonator consisted of a mass block with mass $m = 0.0054$ kg and a linear spring with stiffness $k = 8746$ N/m. Therefore, for the second and third case, the masses of each mass block were $m = 0.0027$ kg and $m = 0.0018$ kg, respectively. For the ABH beam resonator, the widths of the tapered beam of the second and third case were half and one-third of that of the first case with width $t = 0.005$ m, respectively. For clarity, the geometric and material parameters used in the example structure are given again in Table 1. For all cases, the translational degrees of freedom of the TPMS component in directions x and z were constrained for simplicity. The WFE method⁴¹ was used to validate the present method. The stiffness matrix and mass matrix needed by the WFE method were extracted from the finite element model established using ABAQUS. In the finite element modelling, a total of 3128 linear quadrilateral

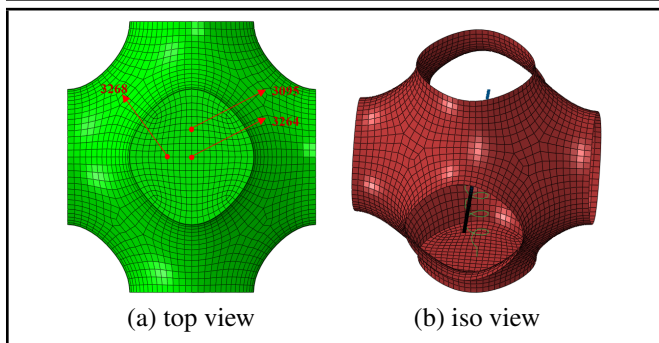


Figure 3. Schematic of connection positions of the resonators, (a) location of the three nodes connected by resonators, (b) Case 1: the ABH component was connected to the TPMS component at the central node of the bottom surface through a spring.

Table 1. Geometric and material parameters used in the studied examples.

	TPMS component	ABH component	Mass-block
Young's modulus, E	2 GPa	70 GPa	\
Density, ρ	1200 kg/m ³	2700 kg/m ³	\
Poisson's ratio, ν	0.3	0.3	\
Thickness, h	0.003 m	$h_0 = 1/400$ m, $h_{tip} = 1/4000$ m	\
	Connected nodes	Beam width t	Mass m
Case 1	3264	1/200 m	0.0054 kg
Case 2	3095, 3264	1/400 m	0.0027 kg
Case 3	3095, 3264, 3268	1/600 m	0.0018 kg

elements of type S4R was used for the TPMS component, and 56000 linear hexahedral elements of type C3D8R was used for each ABH component.

4.1. With One Resonator

The case of which the resonator is connected at node 3264 was considered firstly, as shown in Fig. 3(b). The first propagational wave was investigated for the primary P-TPMS component, the unit cell with spring-mass resonator and the unit cell with ABH resonator, respectively. The real and imaginary part of the wave number k_p are given in Fig. 4(a) and Fig. 4(b), respectively. As can be seen, for the unit cell with ABH resonator, the results from the present semi-analytical method agree well with the results from the WFE method. Figure 5 shows the dispersion results of the TPMS component embedded with ABH resonator obtained by the present method using different approximation order for the WKB description. As can be seen, the results using third-order approximations are convergent. Therefore, the results of the present method calculated with third-order WKB approximation for the ABH component are adopted in this paper.

The band gap results given in Fig. 4 are presented more clearer in Table 2. For the primary P-TPMS component, there exists two band gaps below 500 Hz. The two band gaps are (198.0 Hz–202.6 Hz) and (412.4 Hz–413.3 Hz). For the unit cell consists of the primary P-TPMS component and spring-mass resonator, three band gaps appear below 500 Hz, i.e. (152.7 Hz–155.0 Hz), (255.1 Hz–257.7 Hz) and (412.4 Hz–413.3 Hz). It can be seen that compared to the primary P-TPMS component, the unit cell with an extra spring-mass resonator has one more band gap, which comes from the dynamic vibration absorber effect, because the natural frequency of the isolated spring-mass system is 202.6 Hz and coincided with one of the natural frequency of the primary P-TPMS com-

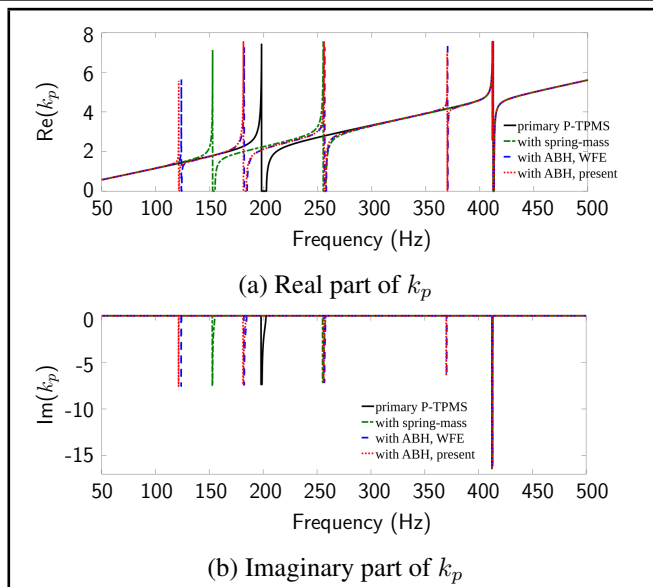


Figure 4. Real and imaginary part of the wave number k_p of the first propagational wave of different unit cells.

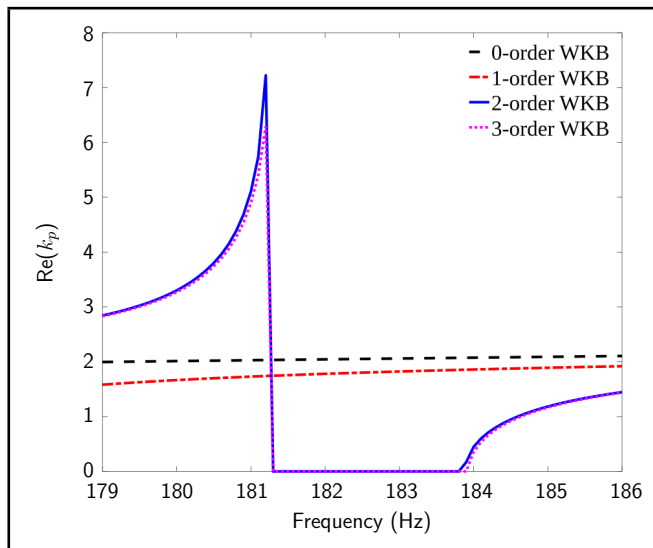


Figure 5. Real part of the wave number k_p of the first propagational wave of the TPMS component embedded with ABH resonator obtained using the present method with different approximation order for the WKB theory.

ponent. The corresponding modal shapes of the primary TPMS component and the TPMS component connected with spring-mass resonator are given in Fig. 6. For the unit cell with ABH resonator, five band gaps appear below 500 Hz, i.e. (121.4 Hz–121.8 Hz), (181.2 Hz–183.9 Hz), (255.9 Hz–257.4 Hz), (369.9 Hz–370.2 Hz) and (412.4 Hz–413.3 Hz). Although the ABH resonator has the same mass with the spring-mass resonator, the unit cell with ABH resonator has two more band gaps than that with the spring-mass resonator below 500 Hz, due to the multimode characteristic of the tapered beam. In addition, total bandwidth of the band gaps increases from 5.6 Hz of the primary P-TPMS component to 5.8 Hz of the unit cell with resonators. Based on the above calculation results, it can be seen that all the above unit cells have the band gap (412.4 Hz–413.3 Hz), which means that, connecting a single resonator at the central node of the bottom surface of the primary P-TPMS component does not change this band gap. This is because the resonator is located at the node lines of

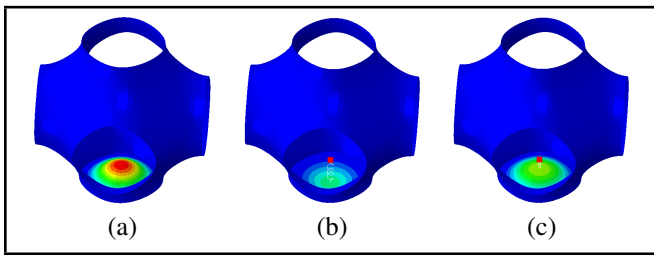


Figure 6. Modal shape of the unit cell obtained using ABAQUS, (a) the primary TPMS component, the natural frequency is 202.6 Hz; (b) TPMS component embedded with the spring–mass resonator, the natural frequency is 154.7 Hz; (c) TPMS component embedded with spring–mass resonator, the natural frequency is 257.0 Hz. The spring–mass system with the same natural frequency is connected at the maximum displacement location of the modal shape at 202.6 Hz of the primary TPMS component, and the new built-up system eliminates the natural mode of the primary component at 202.6 Hz, but produces two new natural modes, one on the left and right sides of 202.6 Hz, i.e. 154.7 Hz and 257.0 Hz.

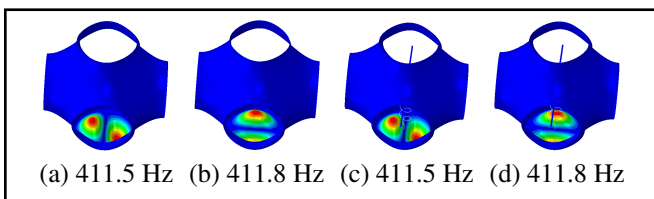


Figure 7. The natural frequencies and corresponding modal shapes of the primary TPMS component and the TPMS component connected by a ABH component at the node lines. The addition of the ABH component does not affect the natural modes of the primary TPMS component at these two natural frequencies.

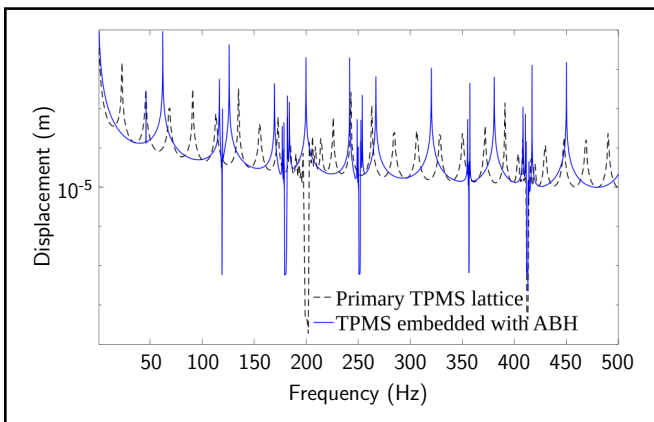


Figure 8. Magnitude of the displacement of the two periodic structure formed by periodically arraying 11 unit cells consist of the primary TPMS and TPMS component embedded with one ABH resonator, respectively.

the two natural modal shapes of the TPMS component corresponding to natural frequencies 411.5 and 411.8 Hz, as can be seen from Fig. 7, which gives the associated modal shapes. Now considered two periodic structures formed by periodically arraying the primary TPMS unit cell and TPMS component embedded with one ABH resonator, respectively. The number of the unit cell for the two structures is 11. Unit point forces are applied uniformly at one end of the periodic structure. And the displacement of one node at the other end of the periodic structure is calculated. Figure 8 shows the magnitude of the displacement of the two periodic structure. As can be seen, the vibration reduction effect shown in the figure is consistent with the band gap results given in Table 2 obtained based on the unit cell.

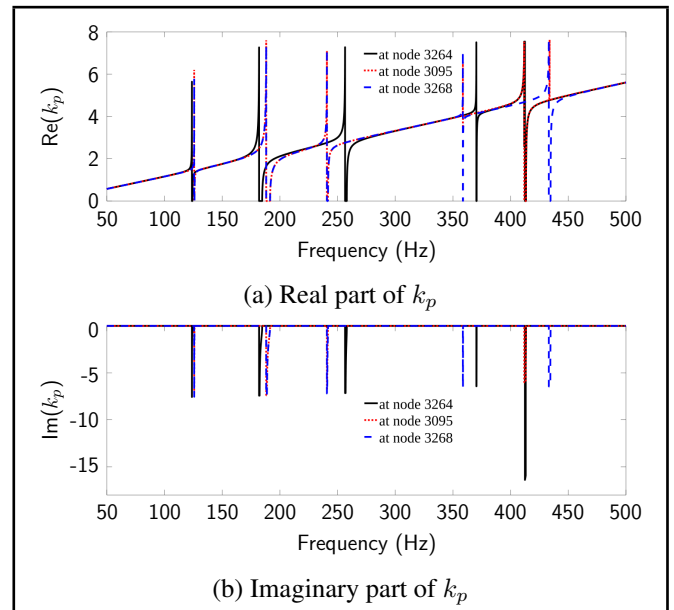


Figure 9. Real and imaginary part of the wave number k_p of the first propagational wave of the unit cell with ABH resonator connected at different nodes.

By changing the parameters of the ABH resonator, five additional cases are considered to investigate the band gap property, and the total width of the band gaps is given in Table 3. As can be seen, the stiffness and mass properties of the ABH resonator significantly influenced the band gap properties. The influence of the position of connection was then investigated. Figure 9 gives the wave number of the first propagational wave of the unit cell with ABH resonator connected at different nodes. As can be seen, for these three cases, although they have similar band gaps at some frequencies, their wave propagation characteristics were very different at most frequencies. For the two cases of which the resonator was connected at nodes 3095 and 3268, the first three band gaps agree well. This was because the two nodes were symmetric in rotation, as shown in Fig. 3(a). It can also be noted that the band gap (412.4 Hz–413.3 Hz) disappeared in the case of which the resonator is connected at node 3268, because the resonator of this case breaks up the natural mode of the primary TPMS component at 411.8 Hz, as can be seen from Fig. 10 and Fig. 7(a, b).

4.2. With Two Resonators

Consider the case of which the two resonators are connected to the primary P-TPMS component at nodes 3264 and 3095. The real and imaginary part of the wave number k_p of the first propagational wave are given in Fig. 11(a) and Fig. 11(b), respectively. As can be seen, for the unit cell with ABH resonator, the results from the present method agree well with the result from the WFE method. Clearer results of the band gaps are given in Table 4. For the unit cell with spring–mass resonators, three band gaps appear below 500 Hz, i.e. (186.8 Hz–189.9 Hz), (310.4 Hz–311.8 Hz) and (411.8 Hz–413.3 Hz). Compared with the case with one spring–mass resonator with the same total mass, although the number of band gaps is the same, the total bandwidth of band gaps is increased from 5.8 Hz to 6.0 Hz, and the first two band gaps move to the right along the frequency axis because that the mass of each mass block is decreased from 0.0054 kg to 0.0027 kg with the spring stiffness unchanged. For the unit cell with

Table 2. Bandgap results of the wave number k_p of the first propagational wave of different unit cells.

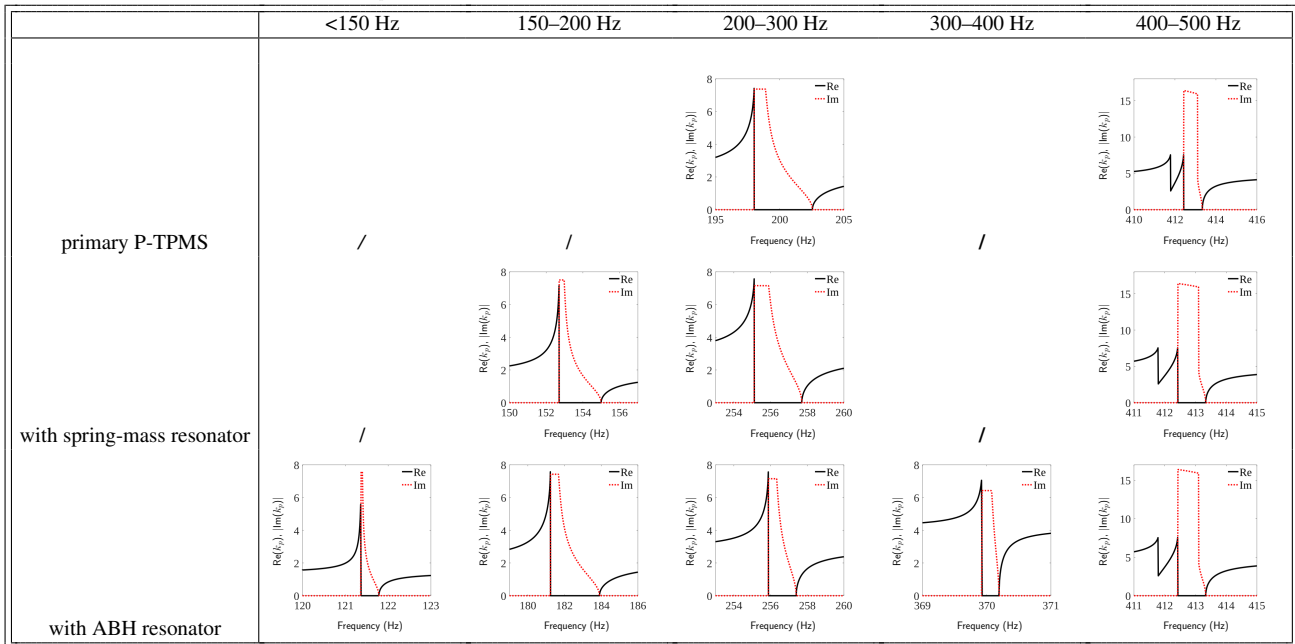


Table 3. Bandgap results of the wave number k_p of the first propagational wave with different ABH configurations.

Case	h_0 (m)	h_{tip} (m)	t (m)	l (m)	ρ (kg/m ³)	Band width (Hz)
0	1/400	1/4000	1/200	1/5	2700	5.8
1	1/100	1/1000	1/100	1/1	2700	5.6
2	1/50	1/500	1/50	1/1	2700	5.2
3	1/25	1/250	1/25	1/1	2700	5.1
4	1/50	1/500	1/50	1/5	2700	7.1
5	1/400	1/4000	1/200	1/5	7800	6.2

two ABH resonators, five band gaps appear below 500 Hz, i.e. (127.5 Hz–127.9 Hz), (186.8 Hz–190.4 Hz), (277.0 Hz–277.6 Hz), (411.8 Hz–413.3 Hz) and (415.0 Hz–415.4 Hz). Compared with the case with one ABH resonator with the same mass, although the number of band gaps is the same, the total bandwidth of band gaps is increased significantly from 5.8 Hz to 6.9 Hz. Compared with the case with two spring–mass resonators with the same total mass, the number and total bandwidth of band gaps of the case with two ABH resonators are increased significantly.

4.3. With Three Resonators

Consider the case of which the three resonators are connected to the primary P-TPMS component at nodes 3264, 3268 and 3095. The real and imaginary part of the wave number k_p of the first propagational wave are given in Fig. 12(a) and Fig. 12(b), respectively. As can be seen, for the unit cell with ABH resonator, the results from the present method agree well with the result from the WFE method. Clearer results of the band gaps are given in Table 5. For the unit cell with spring–mass resonators, three band gaps appear below 500 Hz, i.e. (224.0 Hz–227.6 Hz), (328.7 Hz–329.2 Hz) and (444.7 Hz–446.2 Hz). Compared with the case with two spring–mass resonators with the same total mass, although the number of band gaps is the same, the total bandwidth of band gaps is decreased from 6.0 Hz to 5.6 Hz. For the unit cell with three ABH resonators, nine band gaps appear below 500 Hz, i.e. (129.5 Hz–129.8 Hz), (188.7 Hz–192.5 Hz), (272.5 Hz–272.51 Hz), (284.9 Hz–285.3 Hz), (395.0 Hz–395.1 Hz), (396.7 Hz–397.1Hz), (447.2 Hz–447.5 Hz), (462.7 Hz–462.8 Hz) and

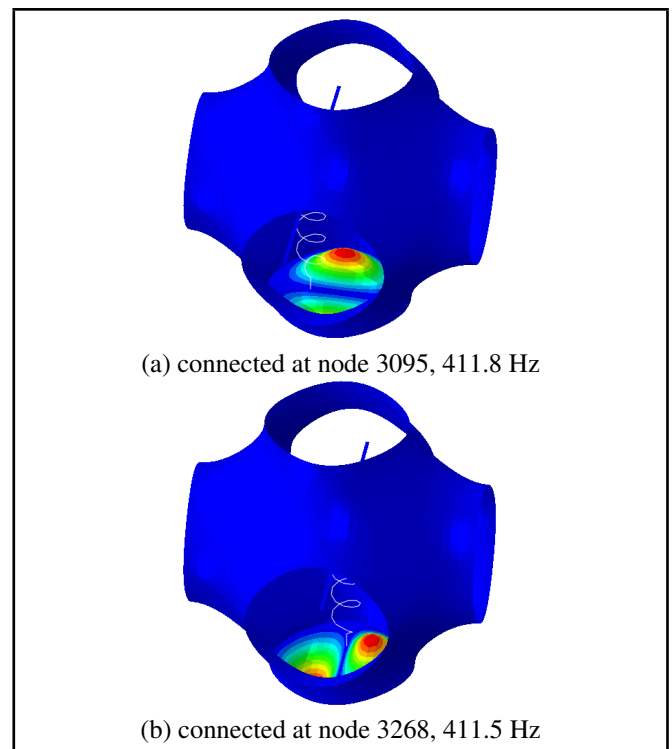


Figure 10. The natural frequencies and corresponding modal shapes of the TPMS component connected by an ABH component at node (a) 3095 and (b) 3268. The addition of the ABH component at node 3268 broke up the natural mode of the primary TPMS component at 411.8 Hz.

(471.6 Hz–471.8 Hz). Compared with the case with two ABH resonators with the same total mass, the number of band gaps was increased from 5 to 9, however, the total bandwidth of band gaps was decreased significantly from 6.9 Hz to 5.6 Hz. Compared with the case with three spring–mass resonators with the same total mass, the number of band gaps of the case with three ABH resonators increases significantly, however, the total bandwidth is unchanged.

Table 4. Bandgap results of the wave number k_p of the first propagational wave of different unit cells.

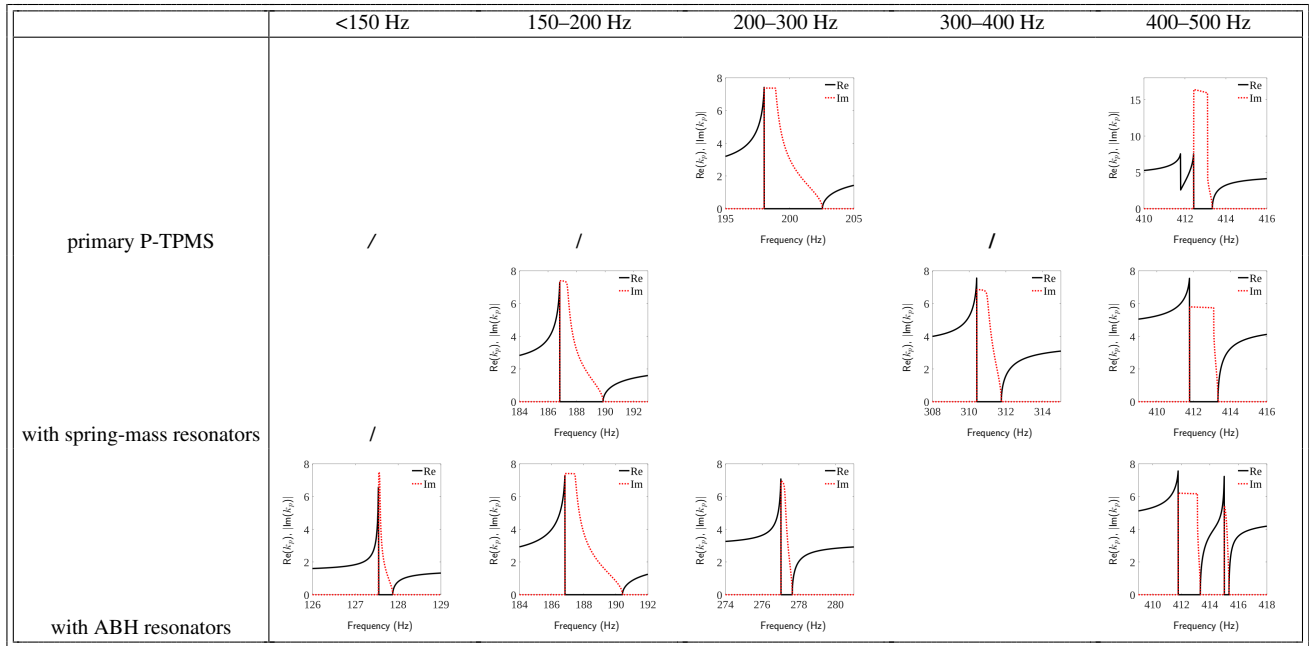


Table 5. Bandgap results of the wave number k_p of the first propagational wave of the unit cells of the primary TPMS component and the TPMS component with spring-mass resonator.

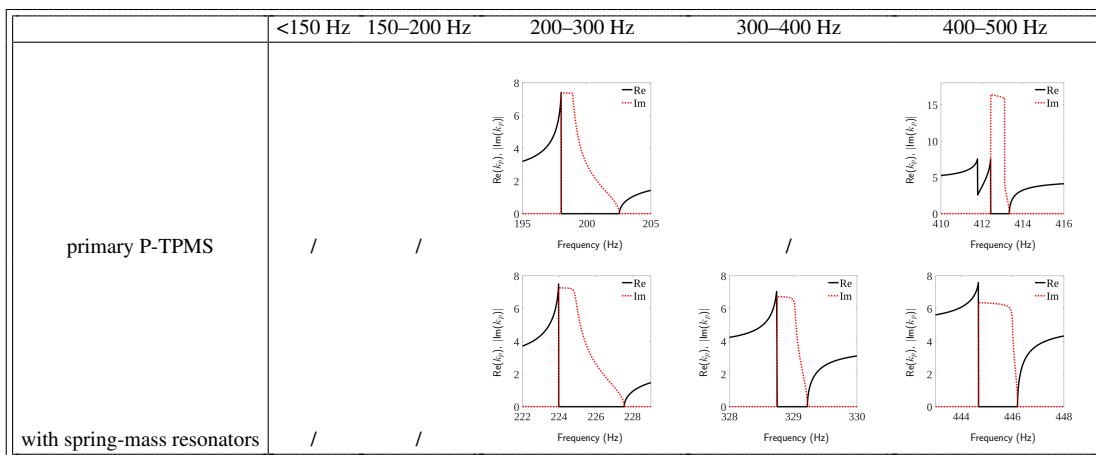
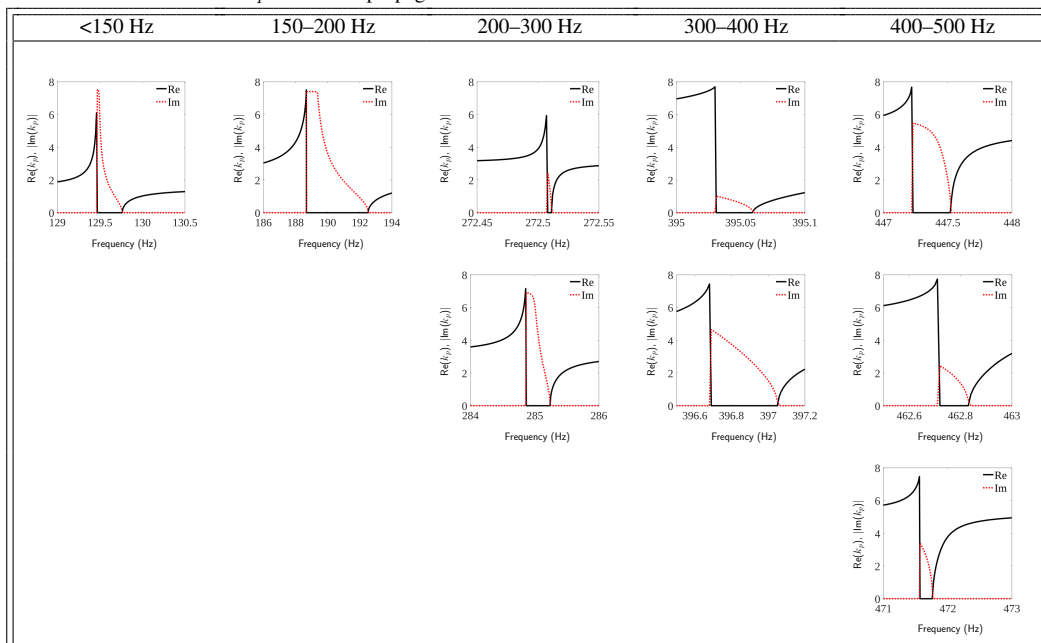


Table 6. Bandgap results of the wave number k_p of the first propagational wave of the unit cell with ABH resonators.



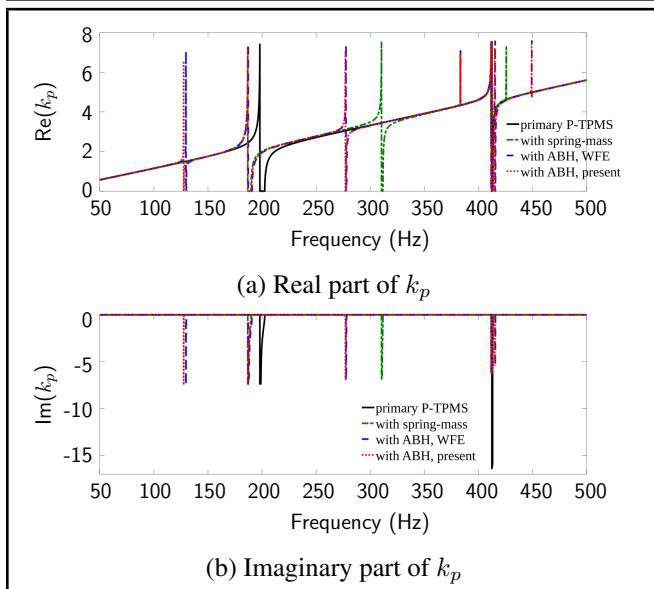


Figure 11. Real and imaginary part of the wave number k_p of the first propagational wave of different unit cells.

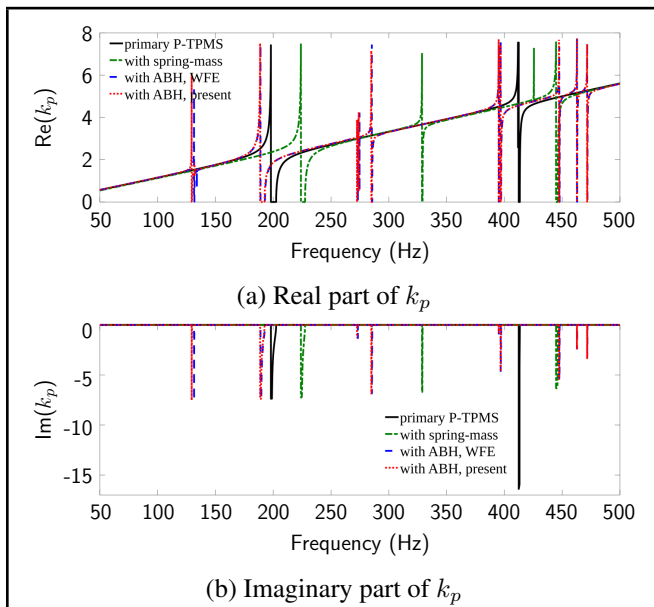


Figure 12. Real and imaginary part of the wave number k_p of the first propagational wave of different unit cells.

5. CONCLUSIONS

Inspired by the porosity of TPMS structure and the application of ABH structure in vibration reduction, a periodic structure with ABH component embedded in P-TPMS component is proposed. A semi-analytical method is developed for the wave propagation analysis of the proposed periodic structure based on the WFE method and the WKB method. Various numerical examples are investigated. For each case with resonators, the total mass of the resonators is kept the same. The main conclusions obtained in these examples are briefly summarized in the following.

Compared with the bandgap properties of the primary P-TPMS component, more band gaps can be obtained by adding resonators to the primary component. The ABH resonator can provide more band gaps than the spring-mass resonator due to the multimode character of the tapered beam. The total

bandwidth of the band gaps is significantly influenced by the connection position of the resonators. For the case with two ABH resonators considered in this paper, the total bandwidth of band gaps is significantly larger than that of the case with mass-spring resonators and the primary component. However, for the case with three ABH resonators considered in this paper, the total bandwidth of band gaps is smaller than that of the cases with fewer resonators and is the same with that of the primary component. Therefore, the number and width of bandgap can be significantly improved by reasonable design of the position and number of the ABH resonators.

It should be noted that the semi-analytical method developed in this paper originated from the need to calculate the wave propagation characteristics of the TPMS structure. However, the proposed method is universal, and it can be directly applied to other complex configurations connected with ABH resonators that are difficult to describe with analytical solutions.

ACKNOWLEDGEMENTS

This work was supported by the National Natural Science Foundation of China (grant number: 12072280).

REFERENCES

- Al-Ketan, O. and Abu Al-Rub, R.K. Multifunctional Mechanical Metamaterials Based on Triply Periodic Minimal Surface Lattices, *Advanced Engineering Materials*, **21**(10), 1900524, (2019). <https://doi.org/10.1002/adem.201900524>
- Gibson, L.J. and Ashby, M.F. *Cellular Solids: Structure and properties*, Cambridge University Press, Cambridge, (1997). <https://doi.org/10.1017/CBO9781139878326>
- Yuan, L., Ding, S.L. and Wen, C. Additive manufacturing technology for porous metal implant applications and triple minimal surface structures: A review, *Bioactive Materials*, **4**(1), 56–70, (2019). <https://doi.org/10.1016/j.bioactmat.2018.12.003>
- Fashanu, O., Rangapuram, M., Abutunis, A., Newkirk, J., Chandrashekhara, K., Misak, H. and Klenosky D. Mechanical performance of sandwich composites with additively manufactured triply periodic minimal surface cellular structured core, *Journal of Sandwich Structures and Materials*, **24**(2), 1133–1151, (2022). <https://doi.org/10.1177/10996362211037012>
- Cai, J.X., Ma, Y.B. and Deng, Z.C. On the effective elastic modulus of the ribbed structure based on Schwarz Primitive triply periodic minimal surface, *Thin-Walled Structures*, **170**, 108642, (2022). <https://doi.org/10.1016/j.tws.2021.108642>
- Qiu, N., Zhang, J.Z., Yuan, F.Q., Jin, Z.Y., Zhang, Y.M. and Fang, J.G. Mechanical performance of triply periodic minimal surface structures with a novel hybrid gradient fabricated by selective laser melting, *Engineering Structures*, **263**, 114377, (2022). <https://doi.org/10.1016/j.engstruct.2022.114377>

- ⁷ Jia, H.R., Lei, H.S., Wang, P.D., Meng, J.X., Li, C.L., Zhou, H., Zhang, X.Y. and Fang, D.N. An experimental and numerical investigation of compressive response of designed Schwarz Primitive triply periodic minimal surface with non-uniform shell thickness, *Extreme Mechanics Letters*, **37**, 100671, (2020). <https://doi.org/10.1016/j.eml.2020.100671>
- ⁸ Ahmed Qureshi, Z., Addin Burhan Al-Omari, S., Elnajjar, E., Al-Ketan, O. and Abu Al-Rub, R. On the effect of porosity and functional grading of 3D printable triply periodic minimal surface (TPMS) based architected lattices embedded with a phase change material, *International Journal of Heat and Mass Transfer*, **183**, 122111, (2022). <https://doi.org/10.1016/j.ijheatmasstransfer.2021.122111>
- ⁹ Abu Al-Rub, R.K., Lee, D.W., Khan, K.A. and Palazotto, A.N. Effective Anisotropic Elastic and Plastic Yield Properties of Periodic Foams Derived from Triply Periodic Schoen's I-WP Minimal Surface, *Journal of Engineering Mechanics*, **146**(5), 04020030, (2020). [https://doi.org/10.1061/\(ASCE\)EM.1943-7889.0001759](https://doi.org/10.1061/(ASCE)EM.1943-7889.0001759)
- ¹⁰ Novak, N., Al-Ketan, O., Krstulović-Opara, L., Rowshan, R., Vesenjak, M. and Ren, Z. Bending behavior of triply periodic minimal surface foam-filled tubes, *Mechanics of Advanced Materials and Structures*, (2022). <https://doi.org/10.1080/15376494.2022.2068207>
- ¹¹ Abueidda, D.W., Abu Al-Rub, R.K., Dalaq, A.S., Lee, D.W., Khan, K.A. and Jasiuk, I. Effective conductivities and elastic moduli of novel foams with triply periodic minimal surfaces, *Mechanics of Materials*, **95**, 102–115, (2016). <https://doi.org/10.1016/j.mechmat.2016.01.004>
- ¹² Tran, P. and Peng, C.X. Triply periodic minimal surfaces sandwich structures subjected to shock impact, *Journal of Sandwich Structures and Materials*, **23**(6), 2146–2175, (2021). <https://doi.org/10.1177/1099636220905551>
- ¹³ Cao, X.F., Zhang, D.F., Liao, B.B., Fang, S.Z., Liu, L.W., Gao, R. and Li, Y. Numerical analysis of the mechanical behavior and energy absorption of a novel P-lattice, *Thin-Walled Structures*, **157**, 107147, (2020). <https://doi.org/10.1016/j.tws.2020.107147>
- ¹⁴ Yáñez, A., Cuadrado, A., Martel, O., Afonso, H. and Monopoli, D. Gyroid porous titanium structures: A versatile solution to be used as scaffolds in bone defect reconstruction, *Materials and Design*, **140**, 21–29, (2018). <https://doi.org/10.1016/j.matdes.2017.11.050>
- ¹⁵ Simsek, U., Arslan, T., Kavas, B., Gayir, C.E. and Sendur, P. Parametric studies on vibration characteristics of triply periodic minimum surface sandwich lattice structures, *The International Journal of Advanced Manufacturing Technology*, **115**(3), 675–690, (2021). <https://doi.org/10.1007/s00170-020-06136-6>
- ¹⁶ Abueidda, D.W., Jasiuk, I. and Sobh, N.A. Acoustic band gaps and elastic stiffness of PMMA cellular solids based on triply periodic minimal surfaces, *Materials and Design*, **145**, 20–27, (2018). <https://doi.org/10.1016/j.matdes.2018.02.032>
- ¹⁷ Viet, N.V., Karathanasopoulos, N. and Zaki, W. Mechanical attributes and wave propagation characteristics of TPMS lattice structures, *Mechanics of Materials*, **172**, 104363, (2022). <https://doi.org/10.1016/j.mechmat.2022.104363>
- ¹⁸ Viet, N.V. and Zaki, W. Free vibration and buckling characteristics of functionally graded beams with triply periodic minimal surface architecture, *Composite Structures*, **274**, 114342, (2021). <https://doi.org/10.1016/j.compstruct.2021.114342>
- ¹⁹ Simsek, U., Akbulut, A., Gayir, C.E., Basaran, C. and Sendur, P. Modal characterization of additively manufactured TPMS structures: comparison between different modeling methods, *The International Journal of Advanced Manufacturing Technology*, **115**(3), 657–674, (2021). <https://doi.org/10.1007/s00170-020-06174-0>
- ²⁰ Yang, W.J., An, J., Chua, C.K. and Zhou, K. Acoustic absorptions of multifunctional polymeric cellular structures based on triply periodic minimal surfaces fabricated by stereolithography, *Virtual and Physical Prototyping*, **15**(2), 242–249, (2020). <https://doi.org/10.1080/17452759.2020.1740747>
- ²¹ Elmadih, W., Syam, W.P., Maskery, I., Chronopoulos, D. and Leach, R. Mechanical vibration bandgaps in surface-based lattices, *Additive Manufacturing*, **25**, 421–429, (2019). <https://doi.org/10.1016/j.addma.2018.11.011>
- ²² Jiang, W.F., Yin, M., Liao, Q.H., Xie, L.F. and Yin, G.F. Three-dimensional single-phase elastic metamaterial for low-frequency and broadband vibration mitigation, *International Journal of Mechanical Sciences*, **190**, 106023, (2021). <https://doi.org/10.1016/j.ijmecsci.2020.106023>
- ²³ Liu, Z.Y., Zhang, X.X., Mao, Y.W., Zhu, Y.Y., Yang, Z.Y., Chan, C.T. and Sheng P. Locally resonant sonic materials, *Science*, **289**(5485), 1734–1736, (2000). <https://doi.org/10.1126/science.289.5485.1734>
- ²⁴ Sang, S., Sandgren, E. and Wang, Z.P. Wave attenuation and negative refraction of elastic waves in a single-phase elastic metamaterial, *Acta Mechanica*, **229**(6), 2561–2569, (2018). <https://doi.org/10.1007/s00707-018-2127-1>
- ²⁵ Xiao, Y., Wen, J.H. and Wen, X.S. Flexural wave band gaps in locally resonant thin plates with periodically attached spring-mass resonators, *Journal of Physics D: Applied Physics*, **45**(19), 195401–195412, (2012). <https://doi.org/10.1088/0022-3727/45/19/195401>
- ²⁶ Miranda, E.J.P., Nobrega, E.D., Rodrigues, S.F., Aranas, C. and Dos Santos, J.M.C. Wave attenuation in elastic metamaterial thick plates: analytical, numerical and experimental investigations, *International Journal of Solids and Structures*, **204**, 138–152, (2020). <https://doi.org/10.1016/j.ijsolstr.2020.08.002>

- ²⁷ Chen, H., Li, X.P., Chen, Y.Y. and Huang, G.L. Wave propagation and absorption of sandwich beams containing interior dissipative multi-resonators, *Ultrasonics*, **76**, 99-108, (2017). <https://doi.org/10.1016/j.ultras.2016.12.014>
- ²⁸ Zuo, S.G., Ni, T.X., Wu, X.D. and Fan, J.L. Studies of band gaps in flexural vibrations of a locally resonant beam with novel multi-oscillator configuration, *Journal of Vibration and Control*, **23**(10), 1663–1674, (2017). <https://doi.org/10.1177/1077546315598032>
- ²⁹ Mei, C. A wave-based analytical solution to free vibrations in a combined euler–bernoulli beam/frame and a two-degree-of-freedom spring–mass system, *Journal of Vibration and Acoustics*, **140**(6), 061001-1, (2018). <https://doi.org/10.1115/1.4039961>
- ³⁰ Ma, Y.B. and Deng, Z.C. A semi-analytical method for the dispersion analysis of orthotropic composite plates with periodically attached acoustic black hole resonators, *Applied Mathematical Modelling*, **110**, 562–582, (2022). <https://doi.org/10.1016/j.apm.2022.06.013>
- ³¹ Mironov, M.A. Propagation of a flexural wave in a plate whose thickness decrease smoothly to zero in a finite interval, *Soviet physics Acoustics*, **34**(3), 318–319, (1988).
- ³² Krylov, V.V. and Tilman, F.J.B.S. Acoustic ‘black holes’ for flexural waves as effective vibration dampers, *Journal of Sound and Vibration*, **274**(3–5), 605–619, (2004). <https://doi.org/10.1016/j.jsv.2003.05.010>
- ³³ Deng J., Xu Y.X., Guasch O., Gao N.S., Tang L.L. and Guo W.J. A wave and Rayleigh-Ritz method to compute complex dispersion curves in periodic lossy acoustic black holes, *Journal of Sound and Vibration*, **546**, 117449, (2023). <https://doi.org/10.1016/j.jsv.2022.117449>
- ³⁴ Deng J., Guasch O., Maxit I., and Gao N.S. An artificial spring component mode synthesis method for built-up structures, *International Journal of Mechanical Sciences*, **243**, 108052, (2023). <https://doi.org/10.1016/j.ijmecsci.2022.108052>
- ³⁵ Deng J., Xu Y.X., Guasch O., Gao N.S. and Tang L.L. Nullspace technique for imposing constraints in the Rayleigh-Ritz method, *Journal of Sound and Vibration*, **527**, 116812, (2022). <https://doi.org/10.1016/j.jsv.2022.116812>
- ³⁶ Jia, X.X., Du, Y., Yu, Y. and Zhao, K.M. Vibration Characteristics of Plate Structures Embedded with Acoustic Black Holes and Distributed Dynamic Vibration Absorbers, *International Journal of Acoustics and Vibration*, **24**(3), 531–539, (2019). <https://doi.org/10.20855/ijav.2019.24.31374>
- ³⁷ Ma, L. and Cheng L. Sound radiation and transonic boundaries of a plate with an acoustic black hole, *The Journal of the Acoustical Society of America*, **145**(1), 164, (2019). <https://doi.org/10.1121/1.5081680>
- ³⁸ Karlos, A., Elliott, S.J. and Cheer J. Higher-order WKB analysis of reflection from tapered elastic wedges, *Journal of Sound and Vibration*, **449**, 368–388, (2019). <https://doi.org/10.1016/j.jsv.2019.02.041>
- ³⁹ Romeo, F. and Luongo, A. Invariant representation of propagation properties for bi-coupled periodic structures, *Journal of Sound and Vibration*, **257**(5), 869–886, (2002). doi: 10.1006/jsvi.2002.5065
- ⁴⁰ Russillo, A.F. and Failla, G. On the free vibrations of locally-resonant structures, *Computers & Structures*, **241**, 106356, (2020). <https://doi.org/10.1016/j.compstruc.2020.106356>
- ⁴¹ Dal Poggetto, V.F. and Serpa, A.L. Flexural wave band gaps in a ternary periodic metamaterial plate using the plane wave expansion method, *Journal of Sound and Vibration*, **495**, 115909, (2021). <https://doi.org/10.1016/j.jsv.2020.115909>
- ⁴² Xie, L.X., Xia, B.Z., Liu, J., Huang, G.L. and Lei, J.R. An improved fast plane wave expansion method for topology optimization of phononic crystals, *International Journal of Mechanical Sciences*, **120**, 171–181, (2017). <https://doi.org/10.1016/j.ijmecsci.2016.11.023>
- ⁴³ Song, Y.B., Feng, L.P., Wen, J.H., Yu, D.L. and X.S. Wen Reduction of the sound transmission of a periodic sandwich plate using the stop band concept, *Composite Structures*, **128**, 428–436, (2015). <https://doi.org/10.1016/j.compstruct.2015.02.053>
- ⁴⁴ Mace, B.R., Duhamel, D., Brennan, M.J. and Hinke, L. Finite element prediction of wave motion in structural waveguides, *The Journal of the Acoustical Society of America*, **117**(5), 2835, (2005). <https://doi.org/10.1121/1.1887126>
- ⁴⁵ Yang, Y., Mace, B.R., and Kingan, M.J. Prediction of sound transmission through, and radiation from, panels using a wave and finite element method, *The Journal of the Acoustical Society of America*, **141**(4), 2452–2460, (2017). <https://doi.org/10.1121/1.4977925>
- ⁴⁶ Cotoni, V., Langley, R.S. and Shorter, P.J. A statistical energy analysis subsystem formulation using finite element and periodic structure theory, *Journal of Sound and Vibration*, **318**(4–5), 1077–1108, (2008). <https://doi.org/10.1016/j.jsv.2008.04.058>
- ⁴⁷ Al-Ketan, O., Abu Al-Rub, R.K., MSLattice A free software for generating uniform and graded lattices based on triply periodic minimal surfaces, *Material Design & Processing Communications*, **e205**, (2020). <https://doi.org/10.1002/mdp2.205>
- ⁴⁸ Zhong, W.X. and Williams, F.W. On the direct solution of wave propagation for repetitive structures, *Journal of Sound and Vibration*, **181**(3), 485-501, (1995). <https://doi.org/10.1006/jsvi.1995.0153>